Phase-contrast microtomography unveils mechanisms of root colonization by a vascular fungal pathogen

David Turrà

davturra@unina.it

University of Naples “Federico II” https://orcid.org/0000-0002-0687-6754

Valentino Maria Guastaferro

Institute for Sustainable Plant Protection – National Research Council

Stefania Vitale

University of Naples “Federico II”

Lorenzo D'Amico

School of Physics and Astronomy, Monash University

Elena Longo

Elettra – Sincrotrone Trieste S.C.p.A.

Giuliana Tromba

Elettra – Sincrotrone Trieste S.C.p.A.

Morgan Delarue

LAAS-CNRS https://orcid.org/0000-0003-1114-298X

Matteo Lorito

University of Naples “Federico II”

Luigi Di Costanzo

University of Naples “Federico II”

Biological Sciences - Article

Keywords:

Posted Date: May 12th, 2025

DOI: https://doi.org/10.21203/rs.3.rs-6567296/v1

Additional Declarations: There is **NO** Competing Interest.

Phase-contrast microtomography unveils mechanisms of root colonization by a vascular fungal pathogen

Valentino Maria Guastaferro[1,2], Stefania Vitale[1,3], Lorenzo D'Amico[4,5], Elena Longo[4], Giuliana Tromba[4], Morgan Delarue[6], Matteo Lorito[1], Luigi Di Costanzo[1], David Turrà[1,3,7,8,*]

[1]Department of Agricultural Sciences, University of Naples "Federico II", Via Università 100, 80055, Portici (Na), Italy; [2]Institute for Sustainable Plant Protection – National Research Council, Piazzale E. Fermi 1, 80055, Portici (Na), Italy; [3]Computational and Quantitative Biology Task Force, University of Naples "Federico II", Naples, Italy; [4]Elettra – Sincrotrone Trieste S.C.p.A., , Basovizza, Trieste, 34149, Italy; [5]School of Physics and Astronomy, Monash University, Wellington Road, Clayton, Victoria 3800, Australia; [6]LAAS-CNRS, Université de Toulouse, CNRS, Toulouse, France; [7]Center for Studies on Bioinspired Agro-Environmental Technology, University of Naples "Federico II", Via Università, 100, 80055 Portici, Italy; [8]Bioelectronics Task Force, University of Naples "Federico II", Naples, Italy

Abstract

Soil-borne vascular pathogens pose serious threats to agriculture with complex invasion strategies that remain poorly characterized compared to foliar pathogens[1]. While foliar pathogens like *Magnaporthe oryzae* employ specialized appressoria to penetrate plant surfaces through a combination of mechanical force and enzymatic degradation[2], the invasion mechanisms of vascular pathogens that lack classical appressoria have remained largely theoretical. The nanoscale processes governing root penetration and colonization by these pathogens are particularly challenging to visualize due to technical limitations of conventional microscopy[3-5]. Here we show, using phase-contrast X-ray computed microtomography and advanced microscopy, that *Fusarium oxysporum* (*Fo*) employs distinct mitogen-activated protein kinase (MAPK) cascades to orchestrate root invasion through unprecedented morphological plasticity. We discovered previously undocumented appressoria-like structures that facilitate physical penetration, while demonstrating that *Fo* exhibits remarkable cellular adaptability, reducing hyphal diameter by more than 20-fold (from 5 µm to 220 nm) to navigate confined plant spaces[6-7], a dramatic morphological transition previously thought impossible. By using cellulase-deficient mutants[8], we demonstrate that cellulolytic activity is dispensable for surface breach and submicrometric hyphal colonization, establishing that mechanical force generation rather than enzymatic degradation is the primary determinant of successful host penetration[9-10]. Three-dimensional reconstruction reveals a quantitative correlation between fungal proliferation and progressive embolism formation, with distinct MAPK pathways differentially regulating penetration force generation (Fmk1), osmotic adaptation during apoplastic colonization (Hog1), and directional growth toward vascular tissues (Mpk1). These findings provide a mechanistic framework for vascular wilt pathogenesis and reveal potential targets for controlling these economically devastating plant diseases.

Main

Soil-borne fungal pathogens cause devastating losses in global agriculture, yet the fundamental mechanisms of host penetration and colonization remain largely enigmatic[1,11,12]. Understanding invasion mechanisms requires detailed visualization of infection processes, but conventional microscopy approaches face significant technical

limitations in capturing these dynamics at the root interface where multiple tissue layers and air-filled spaces impede high-resolution imaging[3-5,13].

In stark contrast to well-characterized foliar pathogens such as *Magnaporthe oryzae*, which utilize specialized appressoria to penetrate plant surfaces through a combination of mechanical force and enzymatic degradation[2], the invasion strategies of soil-borne vascular pathogens have remained largely theoretical until now.

Fusarium oxysporum (*Fo*), a devastating vascular wilt pathogen affecting over 100 different crops and causal agent of the recent Panama disease pandemics[11,14], enters host roots through microscopic wounds, cracks, or nanoscale spaces between adjacent epidermal cells[15]. However, the cellular mechanisms underlying root penetration remain unclear since *Fo* lacks classical appressoria.

Here we present the first comprehensive three-dimensional visualization of the infection process in a soil-borne vascular pathogen, revealing previously unobserved mechanisms of host penetration and colonization. By integrating phase-contrast X-ray computed micro tomography (micro-CT) with advanced microscopy, we reveal how *Fo* orchestrates root invasion and colonization through distinct MAPK signaling cascades. By optimizing micro-CT protocols[16], we achieved unprecedented subcellular resolution (0.9 μm^3 voxel size), enabling non-destructive, three-dimensional tracking of the infection process while preserving the structural integrity of the host-pathogen interface. This technical advancement overcomes key limitations of conventional microscopy, particularly the restricted probe penetration and light scattering in air-filled spaces that have historically precluded detailed analysis of belowground infection processes in their native spatial context[5].

Image processing of phase-contrast X-ray micro-CT data distinguished fungal cells from plant tissues while revealing key root anatomical structures in tomato samples (Fig. 1a). Furthermore, this high-resolution imaging approach captured the progressive stages of host invasion by *Fusarium oxysporum* f. sp. *lycopersici* in tomato roots, documenting clear colonization patterns within host tissues at 3 days post inoculation (DPI) with embolism formation increasing significantly by 5 DPI (Fig. 1b; Supplementary Video 1). Micro-CT analysis revealed previously undocumented infection structures in *Fo*: bulbous appressoria-like structures (ALS) generating needle-shaped invasive hyphae (IH) for plant penetration (Fig. 1c-e). This first visualization of such structures in a soil-borne vascular pathogen challenges the paradigm that specialized penetration structures occur exclusively in foliar pathogens. Orthogonal views documented IH emerging from ALS

initially penetrating epidermal cells (Fig. 1d-e), with subsequent colonization occurring predominantly through apoplastic spaces in subepidermal and cortical tissues (Fig. 1g,h). Notably, apoplastic invasion directly corresponded with the formation of air-filled spaces observed in close association with invading hyphae (Fig. 1f), suggesting a causal relationship between fungal colonization and air space generation.

A fundamental challenge for *Fo* during host colonization lies in the dimensional mismatch between its normal hyphal diameter (4-6 μm)[17,18] and the confined plant apoplastic spaces (50 nm-1 μm) or plasmodesmata (50-60 nm)[6,7]. To rigorously assess hyphal morphological plasticity under defined spatial constraints, we used custom-fabricated PDMS microfluidic devices with nanochannels measuring 500-700 nm in width and 20 μm in length. These experiments demonstrated efficient hyphal growth through submicrometric passages for extended distances, comparable to the diameter of a typical plant cell[19], with ALS consistently forming at channel entry points before initiating thin hyphal filaments (Fig. 2a; Extended Data Fig. 1). Using nylon-based artificial membranes with precisely defined pore diameters (ranging from 5 μm to 0.22 μm) alongside poreless cellophane barriers, we documented the fungus's capacity to reduce its hyphal diameter by more than 20-fold, enabling passage through pores as small as 220 nm (Fig. 2b).

To verify these observations and characterize the penetration mechanisms, we employed complementary analytical approaches. Confocal microscopy of fluorescently tagged *Fo* hyphae confirmed that specialized infection structures form during both artificial membrane penetration and plant colonization. Three-dimensional reconstructions revealed ALS and IH formation at sites of cellophane penetration (Fig. 2d), while similar structures were observed penetrating root epidermal cells (Fig. 2e; Extended Data Fig. 2). Further analysis of cellophane-associated fungal structures (Extended Data Fig. 3) demonstrated the remarkable attachment strength of these specialized infection structures. When colonies grown on cellophane were subjected to vigorous washing, bulbous ALS remained firmly anchored to the membrane surface, while surrounding mycelium was completely removed. High-resolution imaging revealed that these persistently attached ALS generated thin hyphal filaments that penetrated vertically through the cellophane matrix (Fig. 2d; Extended Data Fig. 3; Supplementary Video 2). This observation provides compelling evidence for the dual functionality of ALS in both substrate adhesion and generation of invasive hyphae, properties previously attributed primarily to the appressoria of foliar pathogens[20]. To determine whether this invasion

mechanism depends on enzymatic degradation or physical force, we conducted penetration assays using *clr-1*Δ cellulase-defective mutants[8]. Both wild-type *Fo* and *clr-1*Δ mutants successfully breached poreless cellophane membranes (Fig. 2c), demonstrating that cellulolytic activity is dispensable for penetration. These findings collectively challenge the long-standing paradigm that enzymatic breakdown of plant cell walls is essential for fungal invasion in non-appressoria-forming pathogens[9,10].

To elucidate the precise mechanisms underlying embolism development, we employed fluorescence microscopy of KOH-cleared roots stained with propidium iodide (PI) and FITC-wheat germ agglutinin (FITC-WGA). This analysis confirmed that *Fo* preferentially colonizes the apoplastic root space (Fig. 3a; Extended Data Fig. 4), with thin hyphal structures concentrated at intercellular junctions (Fig. 3b). This colonization strategy, also exploited by biotrophic pathogens to suppress host defenses during intercellular invasion[21], appeared mechanically significant in the pathogenesis process. Quantitative fluorescence intensity profiles along defined transects validated the precise positioning of fungal hyphae between adjacent plant cell walls (Fig. 3c), providing evidence for a mechanical wedging mechanism. However, while fluorescence microscopy corroborated the linear growth patterns of hyphae within constrained apoplastic spaces, it failed to provide complete spatial context in central root regions due to poor probe penetration and light scattering in air-filled spaces. This technical limitation highlighted the advantages of micro-CT for comprehensive three-dimensional visualization of the host-pathogen interface throughout the infection process.

Temporal analysis through three-dimensional micro-CT renderings documented the progression of tissue disruption from 3 to 5 DPI (Fig. 3d; Extended Data Fig. 5), revealing a predominant apoplastic colonization strategy with localized instances of symplastic invasion, particularly at sites of initial penetration and advanced infection stages. Quantitative volumetric assessment demonstrated a two-fold increase in fungal abundance between 3 and 5 DPI coinciding with a three-fold increase in air space volume, while root tissue integrity declined progressively (Fig. 3e-g). The temporal and spatial correlation between fungal proliferation and embolism development provides compelling evidence that *Fo* disrupts vascular function through mechanical interference rather than solely through induced host defense responses[12,22]. The quantitative relationship between fungal biomass increase (two-fold) and embolism expansion (three-fold) demonstrates that hyphal colonization physically disrupts cell junctions, creating air-filled cavities that compromise water transport infrastructure. This mechanical model of pathogenesis

directly contributes to the characteristic wilt symptoms observed during disease progression. Notably, to achieve this colonization strategy, *Fo* requires remarkable cellular adaptability, particularly considering the dimensional constraints within plant tissues. In fact, for successful colonization, *Fo* must undergo substantial cell wall remodeling during hyphal constriction, a significant challenge given that fungal cell walls normally constitute 40% of cell volume and range from 50-500 nm in thickness[23,24]. The dramatic morphological variations we documented reveal previously unrecognized mechanisms of cellular plasticity that enable *Fo* to navigate through the complex nanoscale architecture of plant tissues.

To further elucidate the molecular mechanisms regulating the sophisticated physical processes of host invasion and colonization, we conducted a systematic analysis of conserved signaling pathways in *Fo*. Three distinct mitogen-activated protein kinase (MAPK) cascades coordinate fungal responses to environmental stimuli and cellular morphogenesis: Fmk1 (regulating invasive growth and adhesion), Mpk1 (maintaining cell wall integrity and mediating host signal perception), and Hog1 (orchestrating osmotic stress adaptation)[25-27]. These highly conserved signaling modules function as central regulatory hubs that translate external stimuli into precise transcriptional and post-translational modifications, ultimately controlling the complex morphological transitions required for successful host colonization[26]. Three-dimensional micro-CT renderings of tomato roots inoculated with MAPK pathway mutants revealed distinct colonization phenotypes (Fig. 4a; Extended Data Fig. 6). Quantitative volumetric analysis demonstrated significantly reduced fungal colonization in both *fmk1*Δ and *hog1*Δ mutants compared to the wild-type strain, while *mpk1*Δ mutants showed a slightly reduced, however non significantly different, phenotype (Fig. 4b). Notably, *fmk1*Δ exhibited the most dramatic reduction in fungal colonization, indicating a severe invasion defect. Assessment of root tissue integrity confirmed that *fmk1*Δ-infected plants maintained significantly higher structural preservation compared to wild-type infected roots (Fig. 4d), correlating with reduced colonization efficacy. While Fmk1 MAPK signaling is known to be essential for cellophane membrane or plant tissue penetration in *Fo*[28,29], the precise molecular mechanisms linking this pathway to the physiological adaptations required for host colonization remain undefined[26]. Through membrane penetration assays, we demonstrate that genetic disruption of the *fmk1* gene specifically impairs the fungus's ability to breach poreless cellophane membranes while maintaining the capacity to navigate through pre-existing nanopores in nylon membranes (Extended Data Fig. 7a).

This selective penetration defect persisted regardless of incubation duration, as comparative time-course experiments revealed that while wild-type, *mpk1*Δ, and *hog1*Δ strains successfully penetrated cellophane membranes, *fmk1*Δ mutants consistently failed even after extended incubation periods (Extended Data Fig. 8). This penetration deficiency correlates directly with the inability of *fmk1*Δ mutants to form appressoria-like structures and establish robust surface adhesion, demonstrated by fluorescence microscopy analysis where *fmk1*Δ mutants exhibited severely impaired attachment to cellophane membranes compared to the firmly adhering wild-type strain (Extended Data Fig. 7b). These adhesion and morphological defects culminate in compromised mechanical force generation during invasion attempts, evidenced by the absence of organized substrate deformation patterns beneath *fmk1*Δ colonies (Fig. 4e). While previous investigations associated Fmk1 with regulation of plant cell wall-degrading enzymes[28,29], our comprehensive analysis challenges the paradigm that enzymatic digestion represents the primary penetration mechanism. The collective evidence from our cellulase-impaired *clr-1*Δ mutants, nanopore-containing membranes, and detailed microscopic examination of *fmk1*Δ mutants demonstrates that penetration is primarily driven by physical force generation rather than enzymatic degradation. Having established this critical role of Fmk1 in the initial penetration phase, we next examined the contribution of other MAPK pathways to plant infection.

Micro-CT analysis revealed that *mpk1*Δ mutants induced significantly enhanced air space formation in infected roots compared to wild-type infections (Fig. 4c), while exhibiting reduced vascular colonization (Fig. 4a). This phenotype aligns with Mpk1's established role in mediating chemotropic responses to host signals[25]. In the absence of functional Mpk1, hyphae likely lose their ability to sense directional cues necessary for targeted xylem invasion, resulting in disorganized cortical proliferation rather than coordinated vascular colonization. Consequently, *mpk1*Δ strains cause increased tissue disruption despite reduced overall virulence[27], demonstrating Mpk1's critical function in spatial orientation during pathogenesis.

Our analysis of the third MAPK cascade revealed distinct functional specialization during infection. While *hog1*Δ strains successfully initiated penetration, they displayed significantly reduced colonization efficiency (Fig. 4a,b; Extended Data Fig. 6). Unlike *fmk1*Δ mutants, *hog1*Δ strains retained the capacity to form functional infection structures and generate mechanical force, as evidenced by successful cellophane penetration and substrate deformation assays (Extended Data Fig. 9a,b). However, these mutants

exhibited striking pore size-dependent osmosensitivity that directly correlated with the degree of hyphal constriction required. While *hog1*Δ efficiently traversed 5 μm pores across all osmotic conditions, penetration progressively declined with decreasing pore diameter, with complete failure to penetrate 0.22 μm membranes under non-isotonic conditions (Fig. 4f; Extended Data Fig. 9c,d). In contrast, wild-type strains maintained consistent penetration through 5 μm and 0.45 μm pores regardless of osmolarity, failing only at 0.22 μm under extreme hyperosmotic stress. This distinctive phenotype reveals a critical biophysical challenge: as hyphae undergo extreme diameter reduction (from 5 μm to 220 nm), substantial cell wall remodeling creates acute vulnerability to osmotic fluctuations. Such vulnerability requires precise Hog1-dependent osmoregulatory mechanisms[30] particularly when the fungus must simultaneously navigate nanoscale passages while adapting to variable osmotic microenvironments as those encountered during apoplastic colonization.

Overall our findings establish a model where three distinct MAPK cascades orchestrate sequential stages of root invasion (Fig. 4g,h): Fmk1 regulates appressoria-like structure formation and force-dependent penetration, Mpk1 governs chemotropic navigation toward vascular tissues, and Hog1 enables nanoscale apoplastic colonization through osmoregulation during extreme cellular remodeling. This functional specialization allows *Fo* to navigate the physically constrained, osmotically variable microenvironments encountered during plant colonization. The discovery that vascular wilt pathogens can reduce hyphal diameter by over 20-fold while maintaining cellular integrity represents a fundamental advance in understanding fungal invasion strategies.

In addition, our results establish a novel mechanistic framework for vascular wilt pathogenesis that challenges the longstanding paradigm of enzymatic degradation as the primary invasion mechanism. Instead, we demonstrate that successful root colonization requires precisely coordinated mechanical force generation, directional growth control, and osmoadaptive responses, orchestrated via a precisely calibrated regulatory network of distinct MAPK signaling pathways. The identification of these pathway-specific contributions provides potential molecular targets for developing resistance strategies against these economically devastating plant diseases. More broadly, these findings reveal how soil-borne fungi have evolved sophisticated regulatory mechanisms to navigate the complex physical and chemical landscapes of plant roots, offering insights into the evolutionary adaptations that enable microbial pathogens to breach host barriers through non-enzymatic means.

Methods

Fungal Strains and Growth Conditions

The tomato pathogenic isolate *F. oxysporum* f. sp. *lycopersici* (*Fo*) race 2 isolate 4287 (FGSC 9935) was used throughout this study. The cellulase-deficient mutant (Δ*clr1*) and MAPK deletion strains (Δ*fmk1*, Δ*hog1*, and Δ*mpk1*) were derived from the *Fo* 4287 genetic background as previously described[8,25,27,28]. Generation of a *Fo* strain constitutively expressing three copies of the fluorophore Fo-mClover3 (*Fo4287-Fo-mClover3*) under the control of the *Aspergillus nidulans gpda* promoter have been described elsewhere[31,32].

For microconidia production, strains were cultured in Yeast extract Peptone Dextrose (YPD)[33] at 28°C with orbital shaking (160 rpm) for 3-5 days. For selective growth of mutant strains, the culture media were supplemented with the following antibiotics: phleomycin (4 μg/mL) for *Δfmk1*, hygromycin B (55 μg/mL) for *Δmpk1*, *Δclr1*, and *Fo4287-FomClover3*, and a combination of hygromycin B (55 μg/mL) and iprodione (10 μg/mL) for *Δhog1*.Conidia were collected by filtration through a nylon mesh (10 μm pore size) followed by centrifugation (5,000 rpm, 10 min). *Fo* gene data are available in Genbank under the following accession numbers: *fmk1*, FOXG_08140; *hog1*, FOXG_06318; *mpk1*, FOXG_05092; *clr1*, FOXG_ 08626.

Plant Growth and Inoculation

Seeds of the *Fo* susceptible *Solanum lycopersicum* cv., 'San Marzano Nano' (La Semiorto Sementi)[34], were surface sterilized in 20% bleach for 20 minutes, followed by three 20-minute washes with sterile water. Seeds were germinated on sterile filter paper at 28°C for 3-4 days until roots reached 1 cm length (Extended Data Fig. 10a). For inoculation, seedlings were transferred to sterile cellophane sheets overlaid on moistened filter paper. Root infection was performed by carefully spreading a 50 μL microconidia suspension (5×10^5 spores) directly on top of the root surface (Extended Data Fig. 10b). Plants were incubated at 28°C in darkness for 3-5 days before further preparation for X-Ray microtomography or fluorescence microscopy experiments.

Phase Contrast X-ray computed Micro tomography

Root segments (2 cm length) were excised from inoculated plants using sterile razor blades and immediately immersed in 1% (w/v) iodine solution (Sigma) for contrast

enhancement in sterile 2 mL microcentrifuge tubes. Sample immersion was maintained for 30 minutes at room temperature. Using a sterilized metal inoculation loop, the stained root segments were transferred to sterile, heat-sealed 200 µL polypropylene pipette tips containing 100 µL of fresh 1% iodine solution. The upper openings of the pipette tips were sealed with wax tape (Parafilm M®, Sigma) and secured with beeswax in a custom-fabricated aluminium sample holder for synchrotron imaging (Extended Data Fig. 10c).

Phase Contrast X-ray computed Micro tomography (micro-CT) was performed at the SYRMEP (SYnchrotron Radiation for MEdical Physics) beamline at the Elettra synchrotron light source (Trieste, Italy; https://www.elettra.eu/)[35] with the storage ring operating at 2.4 GeV. The white/pink beam setup was used for propagation-based phase-contrast imaging with the following parameters: 1.5 mm silicon filter (average energy 25.5 keV), sample-to-detector distance of 11 cm, and exposure time of 50 ms per projection. Images were acquired using a water-cooled Hamamatsu Orca Flash sCMOS detector (2048 × 2048 pixels, 6.5 µm x 6.5 µm physical pixel size) coupled to a 17 µm thick Gallium Gadolinium Garnet scintillator. An optical magnification system connected to the detector allowed for an effective pixel size of 0.9 µm × 0.9 µm with a field of view of 1.8 mm × 1.8 mm.

For each sample, 1800 radiographic projections were collected over180°, along with 20 flat-field (*i.e.* images without the sample) and 20 dark-field (*i.e.* images without the X-ray beam) images, acquired at the beginning of each micro-CT scan, for normalization. Image reconstruction was performed using SYRMEP Tomo Project software[36].

Before reconstruction using filtered-back projections, Paganin's single-distance phase retrieval[37] was applied to all the flat-fielded projections with a δ/β ratio of 20. All these steps are part of the STP routine. Subsequent image analysis and segmentation were conducted using ImageJ[38], VG Studio MAX (Volume Graphics GmbH, Heidelberg, Germany) or Dragonfly (Object Research Systems, Montreal, Canada) software.

Micro-CT Data Processing and Analysis

To standardize the tomograms for subsequent analysis, we converted them from 32-bit to 16-bit using a value range of -0.003 to 0.005 as the minimum and maximum for the conversion in VG Studio MAX (v3.1.2). This ensured consistent gray-value ranges for cell walls, fungal hyphae, intercellular spaces, and cellular contents across all samples.

To distinguish fungal structures from plant tissues, we then processed the X-ray micro-CT datasets in ImageJ (NIH, version 1.53c). This involved generating Maximum

Intensity Projections (MIPs) from 32 Z-slices (1.075 µm Z-distance), followed by contrast inversion and thresholding to enhance feature discrimination.

Following these initial processing steps, in order to analyze volumes of air-filled vessels and plant- or fungal-occupied spaces were quantitatively compared across time points and fungal genotypes using Dragonfly 2022.2 (Comet Technologies Canada Inc., Montreal, Canada; available at https://www.theobjects.com/dragonfly). This analysis was conducted on an Agando workstation (Intel Core i5-10600KF, 4.8 GHz, 64 GB RAM, NVIDIA GeForce RTX3060 12GB GPU).

Initial visualization, combining window level adjustment and histogram-based intensity profiling, enabled the precise identification of distinct gray-value thresholds. These thresholds, consistently applied across all images and samples, were used to create regions of interest (ROIs) corresponding to plant tissues, fungal structures, and air spaces, thereby minimizing bias.

For volumetric analysis, a cylindrical ROI with dimensions 0.150 mm in diameter and 0.180 mm in height (volume of 0.020 mm3) was precisely aligned along the root's Z-axis. This cylindrical ROI encompassed two-thirds of the root's cross-sectional area. Within this defined volume, volumetric analysis of segmented ROIs was performed to quantify the spatial distribution of air-filled intercellular spaces and tissue-occupied regions. For robust comparison across samples, total voxel counts for air-filled and tissue-occupied regions were normalized to their respective cylindrical reference ROI volumes. To achieve statistical significance and account for potential variability within each sample, volumetric analyses were conducted using four independent cylindrical ROIs per root.

Fungal Penetration Assays

Fungal penetration was assessed by placing autoclaved cellophane (colorless; Manipulados Margok) or nylon membranes (Poretics, pore size 5 µm; CHMlab, pore size 0.45 and 0.22 µm) on minimal medium (MM)[39] supplemented with KCl (0.3-1.1 M) to generate defined osmotic pressures (1.38-5.06 MPa). Membrane centers were inoculated with a spore suspension of selected fungal strains (4 µL containing 5×10^4 microconidia) and incubated at 28°C for 3 days. Penetration was evaluated by removing membranes and imaging plates after 24 h additional incubation. Where specified, colonies were imaged both before membrane removal and after the additional incubation period.

To test *Fo* invasion, we used previously published chemostat devices which consist in conidial culture chambers (50 µm x 50 µm x 10 µm, lxLxh), connected to feeding

chambers through a set of narrow channels (0.5 µm or 0.7 µm x 1 µm in cross section, 20 µm in length). The polydimethylsiloxane (PDMS) devices were molded on silicon wafer made from classical photolithography, and plasma-bounded to #1 thickness glass slide as previously described[40]. In each experiment conidial culture chambers were loaded with a fungal suspension (2.5×10^6 conidia mL^{-1}) and incubated at 28°C for up to 48 h before imaging.

Osmotic pressures were calculated using van 't Hoff's equation (π = MRT, using the OMNI calculator software; https://www.omnicalculator.com/chemistry/osmotic-pressure). Each experiment included three replicates and was performed three times.

Force Propagation Analysis

To assess fungal-generated mechanical forces, we monitored substrate deformation caused by *Fo* growth. Cellophane membranes overlaid on MM were centrally inoculated with a microconidia solution (4 µL containing 5×10^4 spores) from wild-type or MAPK mutant strains and incubated at 28°C for 4 days. After colony and membrane removal, substrate deformation was analyzed in 1-cm transverse sections using a THUNDER Imager 3D system (Leica DM6 B) with ×10/0.8 NA dry objective and K5 camera (Leica Microsystems). Composite images were generated from individual captures by using the LAS X 5.3.0 software. Each experiment included three replicates and was performed twice.

Microscopy and image analysis

Root samples were cleared according to previously described protocols with slight modifications[41]. Briefly, 2 cm root segments were immersed in 96% ethanol for 24–36 hours, followed by treatment with a 10% KOH solution until imaging. The segments were then washed three times in PBS (pH 7.4) and then stained with a PBS based mix of propidium iodide (PI; 0.5 mg/mL; Sigma-Aldrich) and FITC-conjugated wheat germ agglutinin (FITC-WGA; 5 µg/mL; Sigma-Aldrich) to visualize plant cell walls and fungal chitin, respectively. Initial low-resolution imaging was performed using an Axio Zoom.V16 stereomicroscope (Zeiss) equipped with a 16×/0.25 NA objective. High-resolution confocal imaging was performed using a Leica Stellaris 5 equipped with White Light Laser (WLL) and Acoustic-Optical Beam Splitter (AOBS). The WLL was tuned to 488 nm and 561 nm for simultaneous excitation, with emission collected at 498-551 nm (FITC-WGA) and 661-796 nm (PI) using Power HyD S detectors. Z-stack images were

acquired with a HC PL APO 63x/1,40-0,60 oil objective and processed using LAS X software (version 5.3.0, Leica Microsystems), with brightness and contrast adjustments applied equally across samples. The acquired Z-stacks were rendered in 3D by using the LAS X software (version 4.2, Leica Microsystems).

For penetration and fungal adhesion assays, cellophane membranes were spot-inoculated centrally as described above and incubated at 28°C for 3 days. Single Z-plane or Z-stack images were acquired either using the same confocal settings or on a THUNDER Imager 3D Tissue system (Leica DM6 B) with K5 sCMOS camera using a HC PL APO 63x/1,40-0,60 oil objective, before and after membrane removal or after vigorously washing under tap water while scraping off the mycelial mat. Image analysis was performed using ImageJ (NIH, version 1.53c) to quantify relative fluorescence intensities and assess fungal distribution patterns along plant cell junctions and within root tissues.

Quantification and Statistical Analysis

For quantitative volumetric analysis of micro-CT data, cylindrical regions of interest (ROI) (radius 0.15 mm, height 0.18 mm; volume 0.020 mm^3) were consistently positioned along the root's Z-axis from tomographic datasets (n=4 independent regions per treatment). Root integrity was calculated as the absolute volume (in mm^3) of intact tissue (sum of cytoplasm and cell wall volumes) within each ROI. Fungal colonization and air space distribution were similarly quantified through threshold-based segmentation, with total voxel counts for each component normalized to their respective cylindrical reference ROI volumes. For fluorescence microscopy, relative intensities of FITC-WGA and PI signals were measured along cell wall junctions and within plant tissues using the line-scan analysis function in ImageJ. Fungal colonization patterns were classified as intracellular or intercellular based on relative positioning of fungal hyphae to plant cell walls. Under osmotic stress conditions, fungal penetration efficiency through nylon membranes was quantified by measuring mean gray values in areas under fungal colonies at different KCl concentrations (0.3-1.1 M) using ImageJ. Statistical analyses were performed using GraphPad Prism. Data are presented as mean ± s.d. Significance was determined by one-way ANOVA with Tukey's post-hoc test (*P < 0.05, **P < 0.01, ****P < 0.0001).

Data Availability

Raw imaging data and analysis scripts are available from the corresponding authors upon request.

References

1. Katan, J. Diseases caused by soilborne pathogens: biology, management and challenges. *Journal of Plant Pathology* **99**, 305-315 (2017).
2. Cruz-Mireles, N., Eseola, A. B., Osés-Ruiz, M., Ryder, L. S. & Talbot, N. J. From appressorium to transpressorium-Defining the morphogenetic basis of host cell invasion by the rice blast fungus. *PLoS Pathog.* **17**, e1009779, doi:10.1371/journal.ppat.1009779 (2021).
3. de Wit, J., Tonn, S., Shao, M.R., Van den Ackerveken, G. & Kalkman, J. Revealing real-time 3D in vivo pathogen dynamics in plants by label-free optical coherence tomography. *Nat. Commun.* **15**, 8353, doi:10.1038/s41467-024-52594-x (2024).
4. Piovesan, A., Vancauwenberghe, V., Van De Looverbosch, T., Verboven, P. & Nicolaï, B. X-ray computed tomography for 3D plant imaging. *Trends Plant Sci.* **26**, 1171-1185, doi:10.1016/j.tplants.2021.07.010 (2021).
5. Czymmek, K. J., Duncan, K. E. & Berg, H. Realizing the Full Potential of Advanced Microscopy Approaches for Interrogating Plant-Microbe Interactions. *Mol. Plant Microbe Interact.* **36**, 245-255, doi:10.1094/mpmi-10-22-0208-fi (2023).
6. Peters, W. S., Jensen, K. H., Stone, H. A. & Knoblauch, M. Plasmodesmata and the problems with size: Interpreting the confusion. *J. Plant Physiol.* **257**, 153341, doi:10.1016/j.jplph.2020.153341 (2021).
7. Hohm, T. *et al.* Plasma membrane H(+) -ATPase regulation is required for auxin gradient formation preceding phototropic growth. *Mol. Syst. Biol.* **10**, 751, doi:10.15252/msb.20145247 (2014).
8. Gámez-Arjona, F. M. *et al.* Impairment of the cellulose degradation machinery enhances *Fusarium oxysporum* virulence but limits its reproductive fitness. *Sci. Adv.* **8**, eabl9734, doi:doi:10.1126/sciadv.abl9734 (2022).
9. Mendgen, K., Hahn, M. & Deising, H. Morphogenesis and mechanisms of penetration by plant pathogenic fungi. *Annu. Rev. Phytopathol.* **34**, 367-386, doi:https://doi.org/10.1146/annurev.phyto.34.1.367 (1996).
10. Geoghegan, I., Steinberg, G. & Gurr, S. The role of the fungal cell wall in the infection of plants. *Trends in Microbiol* **25**, 957-967, doi:10.1016/j.tim.2017.05.015 (2017).
11. Dean, R. *et al.* The Top 10 fungal pathogens in molecular plant pathology. *Mol. Plant Pathol.* **13**, 414-430, doi:10.1111/j.1364-3703.2011.00783.x (2012).
12. Yadeta, K. A. &, Thomma J. B. P. The xylem as battleground for plant hosts and vascular wilt pathogens. *Front Plant Sci.* **4**, 97, doi:10.3389/fpls.2013.00097 (2013).
13. Duncan, K. E., Czymmek, K. J., Jiang, N., Thies, A. C. & Topp, C. N. X-ray microscopy enables multiscale high-resolution 3D imaging of plant cells, tissues, and organs. *Plant Physiol.* **188**, 831-845, doi:10.1093/plphys/kiab405 (2022).
14. Vitale, S. & Turrà, D. NO: from plant immunity to fungal virulence factor. *Trends Plant Sci.*, doi:https://doi.org/10.1016/j.tplants.2025.03.021 (2025).
15. Pérez-Nadales, E. & Di Pietro, A. The membrane mucin Msb2 regulates invasive growth and plant infection in Fusarium oxysporum. *Plant Cell* **23**, 1171-1185, doi:10.1105/tpc.110.075093 (2011).
16. Donato, S. *et al.* Optimization of pixel size and propagation distance in X-ray phase-contrast virtual histology. *J. Instrum.* **17**, C05021, doi:10.1088/1748-0221/17/05/C05021 (2022).
17. Ruiz-Roldán, M. C. *et al.* Nuclear dynamics during germination, conidiation, and hyphal fusion of *Fusarium oxysporum*. *Eukaryot. Cell* **9**, 1216-1224, doi:10.1128/ec.00040-10 (2010).

18. Shahi, S., Beerens, B., Manders, E. M. M. & Rep, M. Dynamics of the Establishment of Multinucleate Compartments in *Fusarium oxysporum*. *Eukaryot. Cell* **14**, 78-85, doi:10.1128/ec.00200-14 (2015).
19. Fridman, Y. *et al*. The root meristem is shaped by brassinosteroid control of cell geometry. *Nat. Plants* **7**, 1475–1484, https://doi.org/10.1038/s41477-021-01014-9 (2021).
20. Howard, R.J. & Valent, B. Breaking and entering: host penetration by the fungal rice blast pathogen *Magnaporthe grisea*. *Annu. Rev. Microbiol.* **50**, 491-512, doi: 10.1146/annurev.micro.50.1.491 (1996).
21. Doehlemann, G. & Hemetsberger, C. Apoplastic immunity and its suppression by filamentous plant pathogens. *New Phytol.* **198**, 1001-1016, doi:https://doi.org/10.1111/nph.12277 (2013).
22. Beckman, C. H., Mueller, W. C., Tessier, B. J. & Harrison, N. A. Recognition and callose deposition in response to vascular infection in fusarium wilt-resistant or susceptible tomato plants. *Physiol. Plant Pathol.* **20**, 1-10, doi:https://doi.org/10.1016/0048-4059(82)90018-2 (1982).
23. Zhao, L. *et al.* Elastic properties of the cell wall of *Aspergillus nidulans* studied with atomic force microscopy. *Biotechnol. Prog.* **21**, 292-299, doi:10.1021/bp0497233 (2005).
24. Davì, V. *et al.* Systematic mapping of cell wall mechanics in the regulation of cell morphogenesis. *Proc. Natl. Acad. Sci. U S A* **116**, 13833-13838, doi:10.1073/pnas.1820455116 (2019).
25. Turrà, D., El Ghalid, M., Rossi, F. & Di Pietro, A. Fungal pathogen uses sex pheromone receptor for chemotropic sensing of host plant signals. *Nature* **527**, 521-524, doi:10.1038/nature15516 (2015).
26. Turrà, D., Segorbe, D. & Di Pietro, A. Protein kinases in plant-pathogenic fungi: conserved regulators of infection. *Annu. Rev. Phytopathol* **52**, 267-288, doi:10.1146/annurev-phyto-102313-050143 (2014).
27. Segorbe, D., Di Pietro, A., Perez-Nadales, E. & Turrà, D. Three *Fusarium oxysporum* mitogen-activated protein kinases (MAPKs) have distinct and complementary roles in stress adaptation and cross-kingdom pathogenicity. *Mol. Plant Pathol.* **18**, 912-924, doi:10.1111/mpp.12446 (2017).
28. Di Pietro, A., Garcia-MacEira, F. I., Meglecz, E. & Roncero, M. I. A MAP kinase of the vascular wilt fungus *Fusarium oxysporum* is essential for root penetration and pathogenesis. *Mol. Microbiol.* **39**, 1140-1152 (2001).
29. Rispail, N. & Di Pietro, A. *Fusarium oxysporum* Ste12 controls invasive growth and virulence downstream of the Fmk1 MAPK cascade. *Mol. Plant Microbe Interact.* **22**, 830-839, doi:10.1094/MPMI-22-7-0830 (2009).
30. Hohmann, S. Osmotic stress signaling and osmoadaptation in yeasts. *Microbiol Mol. Biol. Rev.* **66**, 300-372, doi:10.1128/mmbr.66.2.300-372.2002 (2002).
31. Redkar, A. *et al.* Conserved secreted effectors contribute to endophytic growth and multihost plant compatibility in a vascular wilt fungus. *Plant Cell* **34**, 3214-3232, doi:10.1093/plcell/koac174 (2022).
32. Redkar, A., Di Pietro, A. & Turrà, D. Live-cell visualization of early stages of root colonization by the vascular wilt pathogen *Fusarium oxysporum*. *Methods Mol. Biol.* **2659**, 73-82, doi:10.1007/978-1-0716-3159-1_6 (2023).
33. Sherman, F. Getting started with yeast in *Methods in Enzymology* Vol. 194 3-21 (Academic Press, 1991).
34. Ranesi, M. *et al.*. Field isolates of *Beauveria bassiana* exhibit biological heterogeneity in multitrophic interactions of agricultural importance. *Microbiol. Res.* **286,** 127819, https://doi.org/10.1016/j.micres.2024.127819 (2024).
35. Longo, E. *et al.* SYRMEP beamline: state of the art, upgrades and future prospects. *The European Physical Journal Plus* **139**, 880, doi:10.1140/epjp/s13360-024-05489-1 (2024).

36. Brun, F. *et al.* Enhanced and Flexible Software Tools for X-ray Computed Tomography at the Italian Synchrotron Radiation Facility Elettra. *Fundam. Inform.* **141**, 233-243, doi:10.3233/FI-2015-1273 (2015).
37. Paganin, D., Mayo, S. C., Gureyev, T. E., Miller, P. R. & Wilkins, S. W. Simultaneous phase and amplitude extraction from a single defocused image of a homogeneous object. *J. Microsc.* **206**, 33-40, doi:https://doi.org/10.1046/j.1365-2818.2002.01010.x (2002).
38. Schneider, C. A., Rasband, W. S. & Eliceiri, K. W. NIH Image to ImageJ: 25 years of image analysis. *Nat. Methods* **9**, 671-675, doi:10.1038/nmeth.2089 (2012).
39. Puhalla, J. E. Compatibility reactions on solid medium and interstrain inhibition in *Ustilago maydis*. *Genetics* **60**, 461-474, doi:10.1093/genetics/60.3.461 (1968).
40. Alric, B., Formosa-Dague, C., Dague, E., Holt, L. J. & Delarue, M. Macromolecular crowding limits growth under pressure. *Nat. Phys.* **18**, 411-416, doi:10.1038/s41567-022-01506-1 (2022).
41. Becker, Y., Green, K. A., Scott, B. & Becker, A. M. Artificial inoculation of *Epichloë festucae* into *Lolium perenne*, and visualisation of endophytic and epiphyllous fungal growth. *Bio. Protoc.* **8**, e2990, doi:10.21769/BioProtoc.2990 (2018).
42. Di Pietro, A. & Roncero, M. I. Cloning, expression, and role in pathogenicity of pg1 encoding the major extracellular endopolygalacturonase of the vascular wilt pathogen *Fusarium oxysporum*. *Mol. Plant Microbe Interact.* **11**, 91-98, doi:10.1094/MPMI.1998.11.2.91 (1998).

Supplementary information is linked to the online version of the paper at www.nature.com/nature.

Acknowledgments

This work was supported by grants from the Italian Ministry of Education, University and Research (PRIN-BiPP/2020T58TA3, PRIN 2022-TAKLPAT/2022SC83XK) to M.L and D.T., and from the Università degli Studi di Napoli Federico II (FRA-Line B-2020-TOPOPATH grant PG/2021/0034842) to D.T. V.G. was supported by the Ph.D. program on 'Sustainable agricultural and forestry systems and food security' at Università degli Studi di Napoli Federico II. This study was carried out within the Agritech National Research Center supported by European Union Next-Generation EU (PNRR—MISSIONE 4 COMPONENTE 2, INVESTIMENTO 1.4–D.D. 1032 17/06/2022, CN00000022). The views expressed are those of the authors and not necessarily those of the European Union or European Commission. We acknowledge Elettra Sincrotrone Trieste for providing access to its synchrotron radiation facilities and for financial support to L.D.C. and D.T. (granted proposal no.20210436).

Author contributions

V.G., S.V., and D.T. designed the experiments. V.G., S.V., D.T., L.D.A., M.D., E.L. and L.D.C. carried out the experiments. V.G., S.V., L.D.C., L.D.A. and D.T. analyzed the data. D.T. wrote the manuscript, with contributions from all the authors.

Author information

Reprints and permissions information is available at www.nature.com/reprints.

The authors declare no competing financial interests.

Correspondence and requests for materials should be addressed to D.T. (davturra@unina.it) and L.D.C (luigi.dicostanzo4@unina.it).

Figures

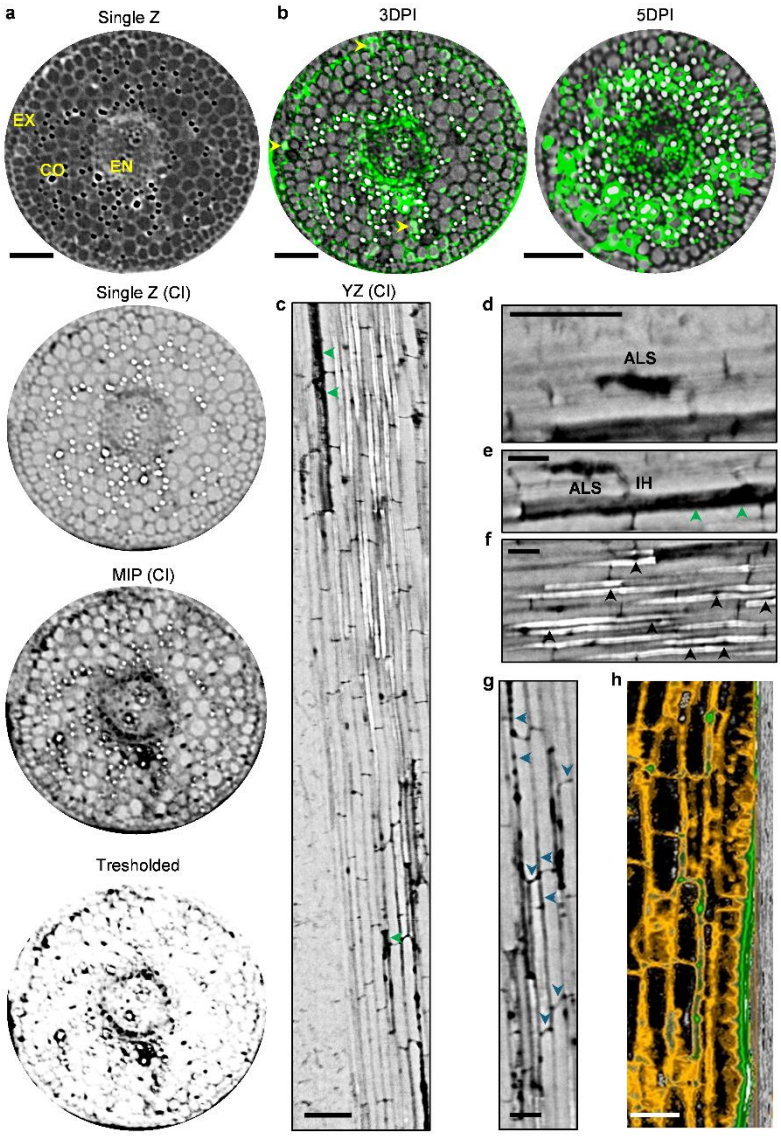

Figure 1. Phase contrast micro-CT imaging of *Fusarium oxysporum* colonized plant roots. a, X-ray microtomography (microCT) cross sections of *Solanum lycopersicum* roots 3-days post inoculation (DPI) with *Fo*. Single Z slices or Maximum Intensity Projections (MIP) of a single stack (32 slices, 28.8 µm Z-distance) were contrast inverted (CI) to visualize sites of fungal growth and thresholded for discriminating fungal cells from background. EX, exodermis; CO, cortex; EN, endodermis. Scale bar, 100 µm. **b**, Segmentation of microCT cross sections of *S. lycopersicum* roots 3 and 5 DPI with *Fo*. Note the increased presence of air-filled vessels (white circles in CI and segmented images) prevalent in heavily colonized root cortex areas. Yellow arrowheads point to rare sites of symplastic fungal growth. Scale bar, 100 µm. **c**, An orthogonal view of the same subvolume shown in **b** (5 DPI) and magnification in **d**-**g** of key fungal colonization steps. Green arrowheads point to sites of symplastic fungal growth. Scale bars, 100 µm (overview), 50 µm (inset). **d**, Visualization of appressoria-like structures (ALS). **e**, A penetration/invasive hyphae (IH) stemming from an ALS invades an underneath plant cell (green arrowheads). **f**, Colocalization of fungal hyphae with air filled spaces (black arrowheads). **g**, Fungal colonization of the plant apoplast (blue arrowheads). **h**, 3D rendering of a segmented microCT acquisition of a tomato root 5 DPI with *Fo* showing fungal colonization (green) of the apoplastic space. Root cell walls and plant cell cytoplasm are colored yellow and black, respectively. Scale bar, 50 µm.

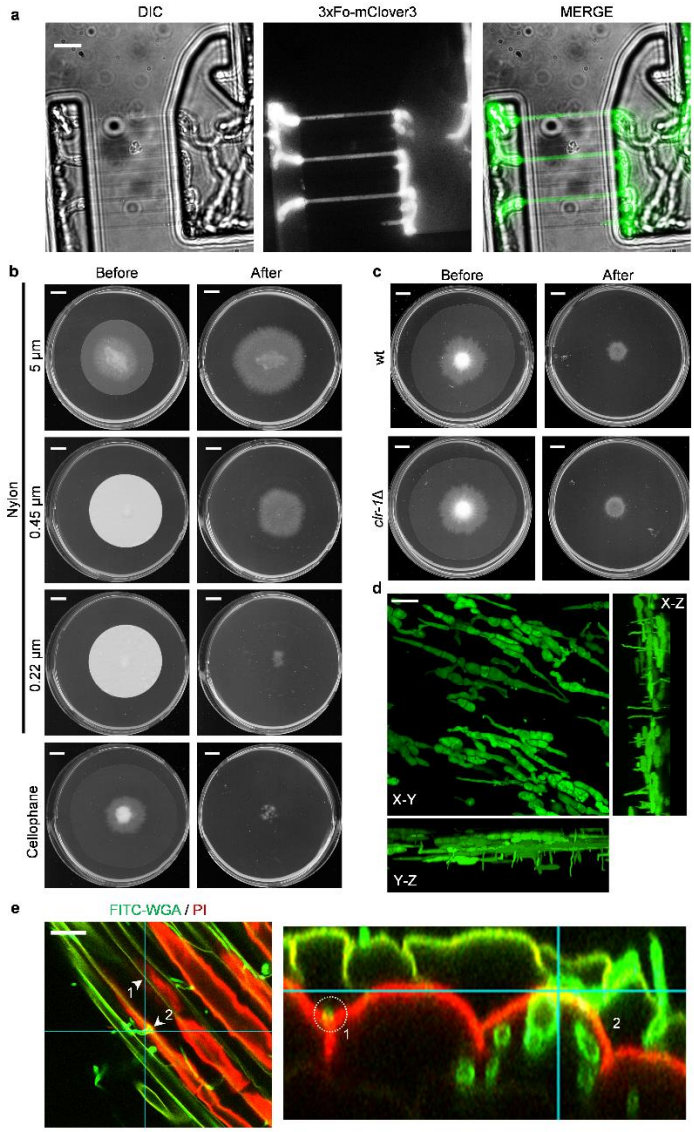

Figure 2. *Fusarium oxysporum* penetration relies on a non-enzymatic process. a, *Fo* hyphae expressing three copies of the cytoplasmic fluorophore Fo-mClover3 (green) traversing 0.7 µm nanochannels in a microfluidic PDMS device. Scale bar, 20 µm. **b**, Representative images of *Fo* invasive growth through pore-containing nylon membranes (5, 0.45, or 0.22 µm pores) or poreless cellophane. Penetration was evaluated by growing fungal colonies for three days on minimal medium (MM) plates overlaid with the corresponding membrane (Before). After membrane removal, plates were incubated for one additional day (After) to visibly detect the presence of penetrated fungal mycelium. **c**, Cellulase production is not required for *Fo* invasive growth on cellophane membranes. Cellophane penetration of the wt strain and of the cellulase-defective mutant *clr-1*Δ was determined after 3 days of incubation on MM plates as described for **b**. Images shown in **b-c** are representatives of three independent experiments each performed in triplicate. Scale bar in **b-c**, 1 cm. **d**, Confocal microscopic images of *Fo* hyphae expressing 3X-Fo-mClover3 imaged directly on a cellophane membrane after 3 days of growth on MM. Images show Z-projections of the in-plane fluorescence (X-Y) and corresponding cross-sections (X-Z and Y-Z) along the Z axis. Note the enlarged bulbous appressoria-like structure (ALS) in X-Y and thinner needle-shaped invasive hyphae (IH) in X-Z and Y-Z sections. Scale bar, 20 µm. **e**, Maximum projection of confocal Z-stack images and corresponding X-Z cross-section of a *Fo*-infected tomato root 3 days post-inoculation. Arrowheads indicate sites of apoplastic fungal invasion (1) and epidermal root cell penetration (2), with ALS formation visible at the penetration site. Inter-cellular hypha is indicated by a white dotted circle. Scale bar, 20 µm.

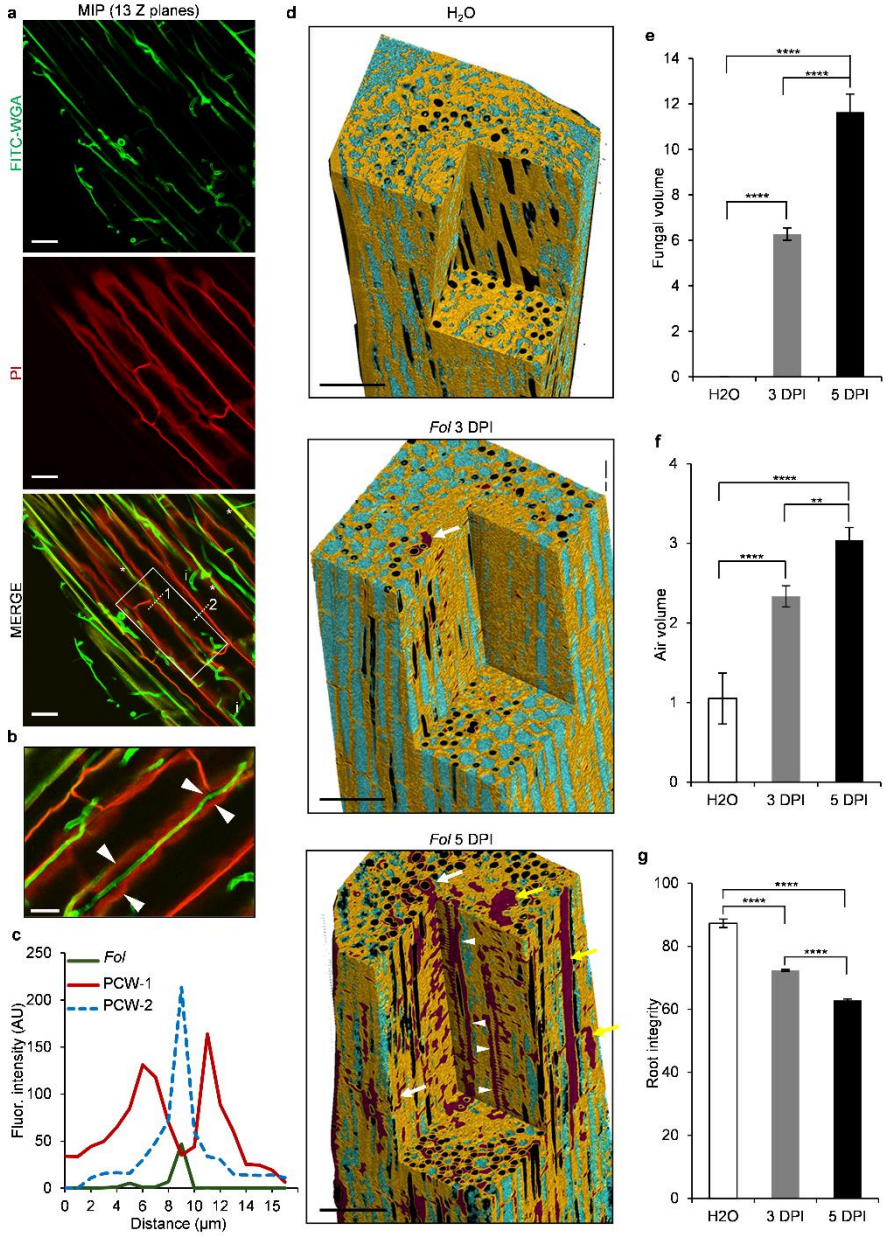

Figure 3. Colonization of tomato roots by *Fusarium oxysporum* primarily relies on apoplast occupancy. a-b, Maximum projection (MIP; 13 Z-sections) of confocal z-stack images of representative KOH-cleared and stained tomato roots 5 days post inoculation (DPI) after inoculation with *Fo*. Root samples were stained with a mix of Propidium iodide (PI; red) and fluorescein isothiocyanate-conjugated wheat germ agglutinin (FITC-WGA; green) to visualize plant cell walls and fungal chitin, respectively. Representative intra- (i) or inter-cellular hyphae (*) are indicated. An area where *Fo* hyphae grow through plant cell junctions is shown at higher magnification in panel (**b**), corresponding to the region marked by a white box in panel **a**. Scale bars, 20 µm (**a**), 10 µm (**b**). **c**, Analysis of relative fluorescence intensities in arbitrary units (AU) of plant cell walls (PCW) and *Fo* hyphae (*Fol*) along the dotted white lines in **a** (merged image). **d**, Magnified view of 3D renderings from Extended Data Fig. 5 showing tomato roots either mock-treated (H_2O) or infected with *Fo* at 3 and 5 DPI. Yellow: cell walls; light blue: cytoplasm; black: air spaces; magenta: fungal hyphae. White and yellow arrows indicate sites of apoplastic and symplastic fungal growth; arrowheads show xylem vessel colonization. Scale bar, 0.1 mm. **e-g**, Quantification of fungal volume (**e**), air spaces (**f**), and root tissue integrity (**g**) from four independent root regions (n=4). Data are mean ± s.d. **P < 0.01, ****P < 0.0001 by one-way ANOVA with Tukey's post-hoc test.

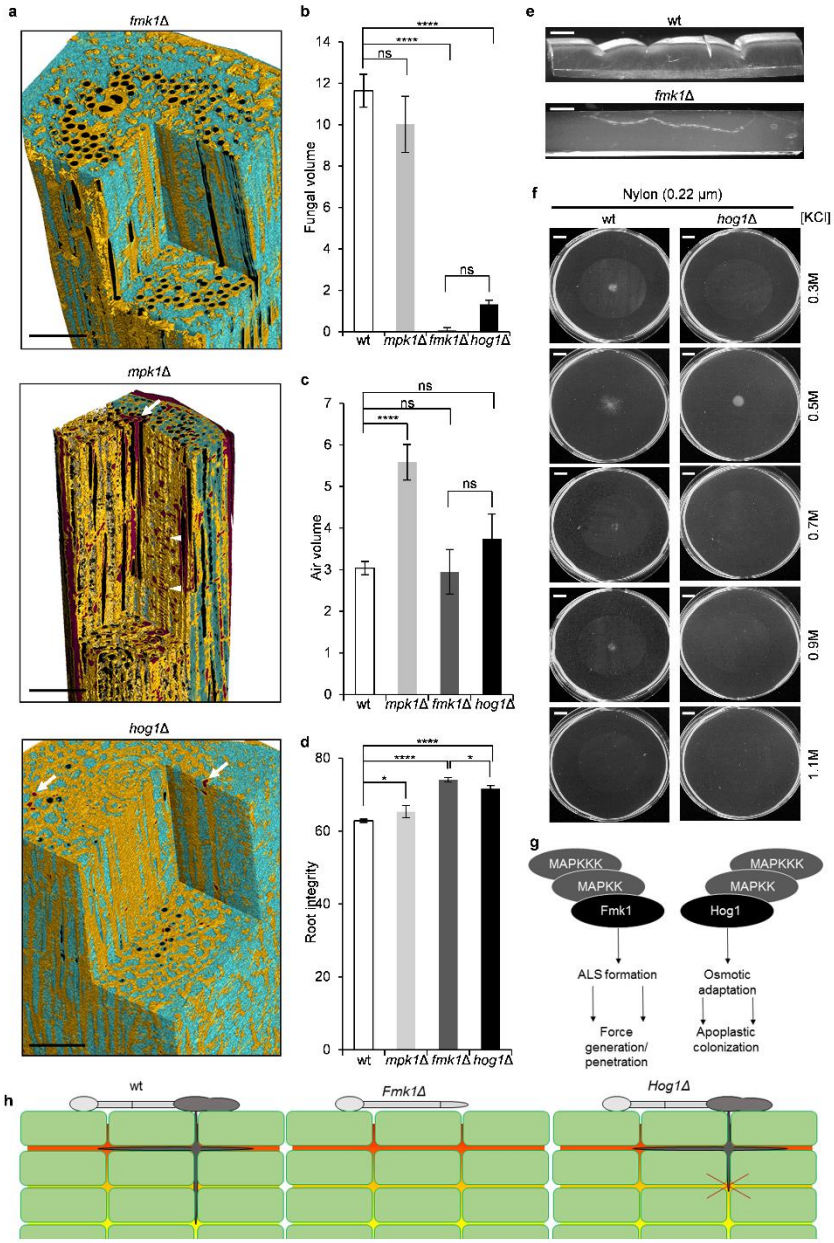

Figure 4. MAPK pathways differentially regulate *F. oxysporum* tissue invasion and root damage. a, 3D synchrotron X-ray micro-CT renderings of tomato roots 5 days post inoculation (DPI) with *F. oxysporum* wild-type or MAPK mutant strains. Yellow: cell walls; light blue: cytoplasm; black: air spaces; magenta: fungal hyphae. White arrows indicate apoplastic colonization; arrowheads show xylem vessel invasion. Scale bar, 0.25 mm. **b**-**d**, Quantification from equal-sized root regions (n=4) showing: **b**, fungal volume; **c**, air space volume as measure of tissue damage; and **d**, root integrity. Data are mean ± s.d. *P < 0.05, ****P < 0.0001 by one-way ANOVA with Tukey's post-hoc test; ns, not significant. **e**, Cross-sections of the growth substrate following cellophane penetration assays at 4 DPI, showing differential substrate deformation beneath wt and *fmk1*Δ colonies. Scale bar, 1 mm. **f**, Membrane penetration under osmotic stress in wt and *hog1*Δ strains. Colonies were grown on media with increasing KCl concentrations (0.3-1.1 M, generating osmotic pressures from 1.38-5.06 MPa) and imaged 24h after membrane removal. Note progressive loss of penetration with increasing osmotic pressure in *hog1*Δ but not in the wt strain. Scale bar, 1 cm. **g**, Schematic representation of MAPK signaling pathways in *Fo* showing Fmk1 regulation of force generation/penetration and Hog1 control of osmotic adaptation required during apoplastic colonization. **h**, Comparative illustration of wt, *fmk1*Δ, and *hog1*Δ invasion phenotypes depicting the distinct mechanical and physiological colonization defects in each mutant.

Extended Data Figures

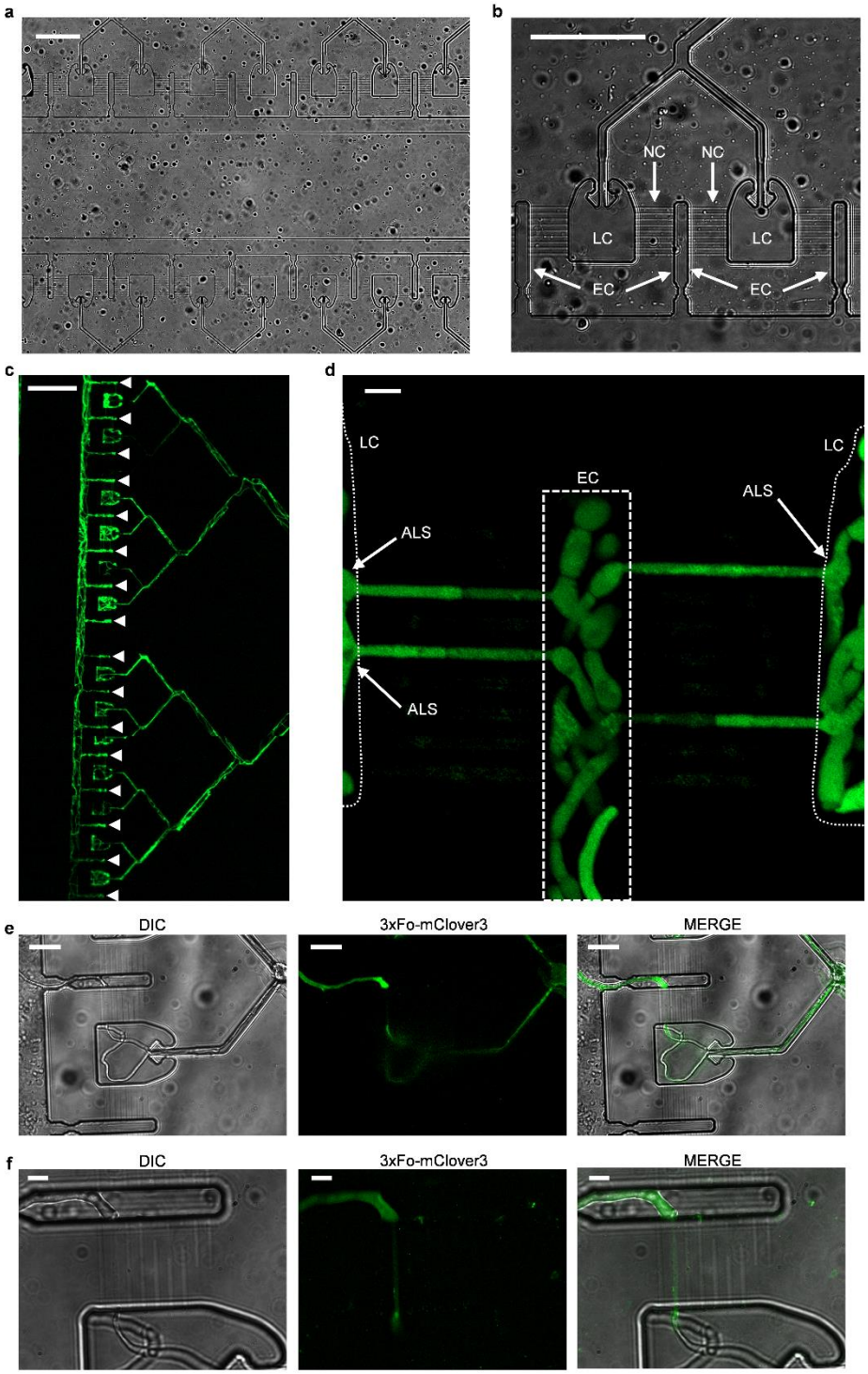

Extended Data Fig. 1. *Fusarium oxysporum* hyphae efficiently explore submicrometric spaces. a-b, Lower (**a**) and higher magnification (**b**) views of the microfluidic device used to track fungal growth through nanometric pores. In **b**, the conidial loading chamber (LC) is connected to two exit chambers (EC), each by an array of nine 700 or 500 nm wide by 20 µm long nanochannels (NC). A single conidium can be captured by the constricted shallow channel above the LC by flowing a fungal suspension containing 2.5 × 10^6 conidia mL^{-1}. Scale bar, 50 µm. **c**, Representative fluorescence microscopy images showing the growth of fungal hyphae (green) from a 3X-Fo-mClover3 expressing *Fo* mutant colonizing the ECs (arrowheads) after crossing the adjacent nanochannels following 40h of growth at 28°C. Note that fungal growth is visible in all ECs. Scale bar, 100 µm. **d**, Maximum projection of confocal Z-stack images

showing 3X-Fo-mClover3 *Fo* hyphae (green) traversing a set of 700 nm wide nanochannels from the microfluidic device in **a**-**c** after 40 hours of incubation. Enlarged bulbous cells (appressoria-like structure; ALS) are indicated by white arrows. Scale bar, 5 μm. **e**-**f**, Maximum projection of representative confocal Z-stack images of a *Fo* hyphae expressing 3X-Fo-mClover3 (green) crossing 500 nm wide nanochannels (**e**) and magnification of it (**f**). Scale bar, 20 μm in **e** and 5 μm in **f**.

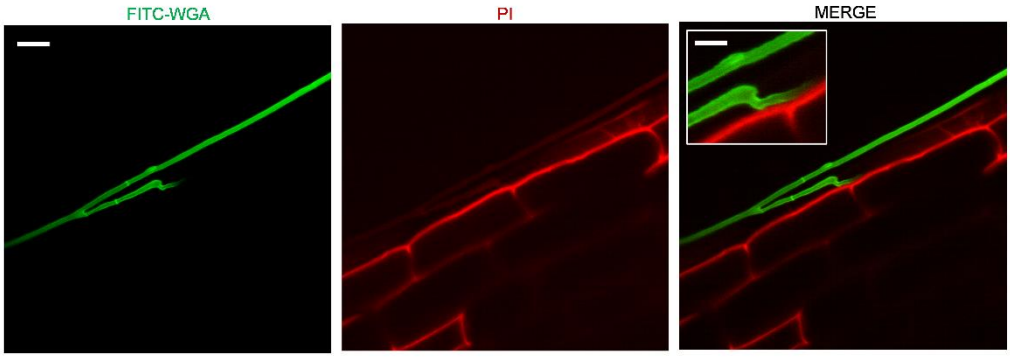

Extended Data Fig. 2. *Fusarium oxysporum* differentiates appressoria-like structures and needle-shaped hyphal filaments on epidermal root surfaces. Maximum projection of confocal Z-stack images showing fungal cell wall (FITC-WGA, green) and plant cell walls (PI, red) of a representative *Fo* hypha penetrating a tomato root epidermal cell. Tomato tissues were imaged 3 days post inoculation (DPI) after root clearing and staining with a PI/FITC-WGA mix. In the merged image (right panel) and inset (white box), a highly polarized hyphal segment emerges from a depolarized hyphal segment (appressoria-like structure) and crosses through the plant cell wall to breach the host epidermal cell surface at the infection point. Scale bar, 20 µm (overview), 10 µm (inset).

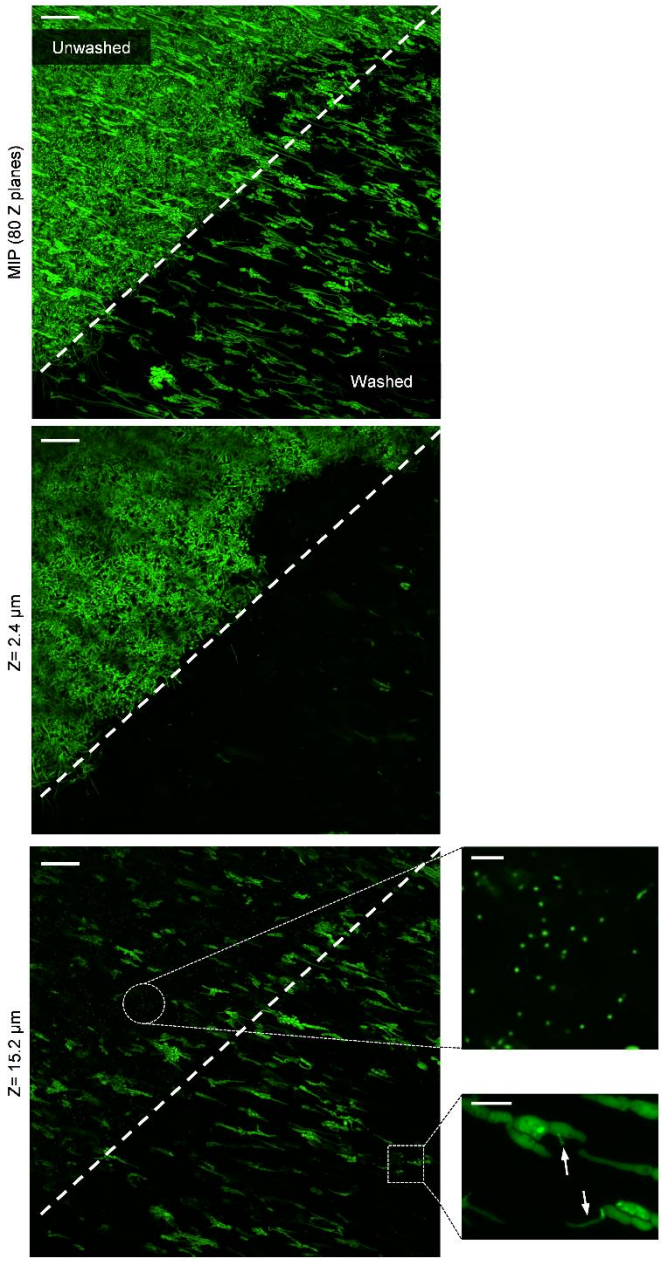

Extended Data Fig. 3. *Fusarium oxysporum* penetrates cellophane membranes by differentiating appressoria-like and needle-shaped hyphal structures. Maximum projection (MIP of 80 Z-sections; 0.4 µm step size) or single plane of confocal Z-stack images of a 3X-Fo-mClover3 expressing *Fo* colony (green) grown on top of a cellophane membrane after 3 d of incubation on a MM plate. Before imaging, one half of the cellophane sheet was vigorously washed under tap water (bottom right) or left unwashed (top left) by scraping off the mycelial colony. Note the presence of enlarged bulbous cells (squared and magnified inset) strongly attached to the cellophane sheet, from which needle-shaped hyphae emerge (arrows) in the washed area. Numerous fluorescent dots (circled and magnified inset) correspond to needle-shaped hyphae vertically penetrating the cellophane membrane. Scale bar, 100 µm (overview), 10 µm (insets).

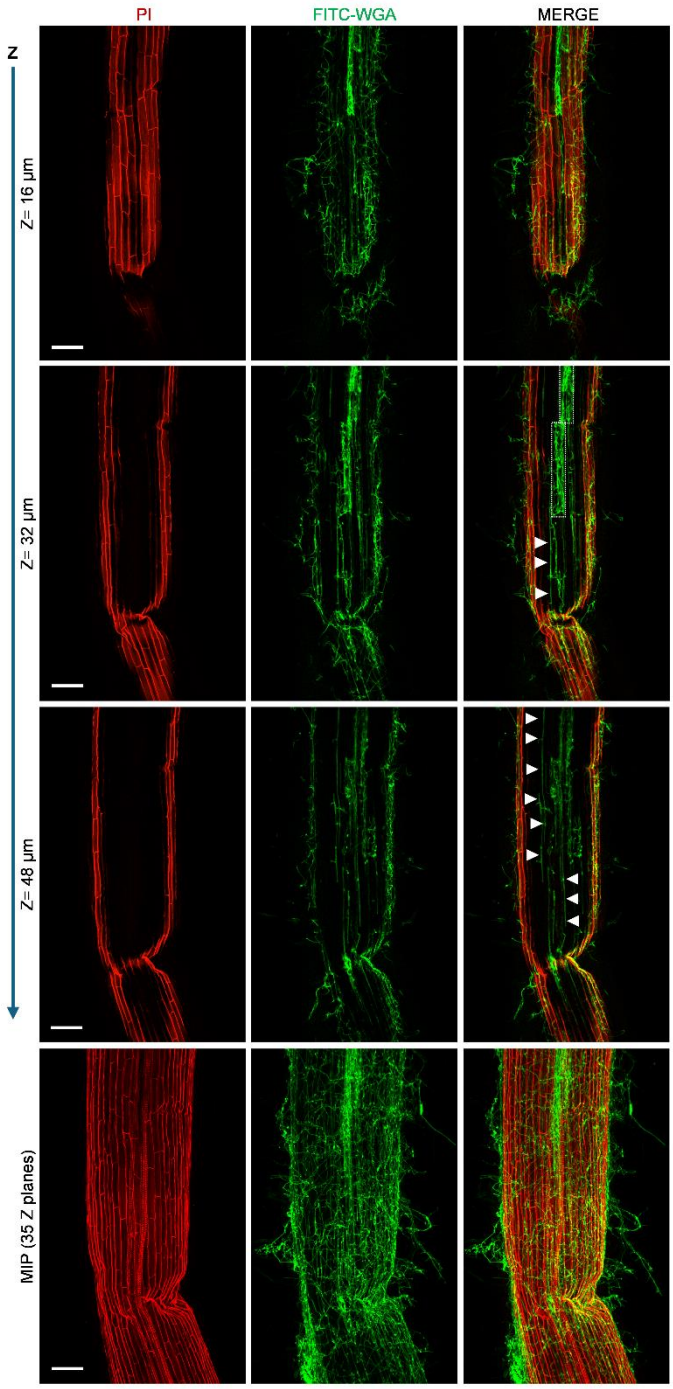

Extended Data Fig. 4. Colonization of tomato roots by *Fusarium oxysporum* primarily relies on apoplast occupancy. Representative fluorescence microscopy images showing the outer root surface (upper view), internal root tissues (inner view), and a maximum intensity projection (MIP; combining 35 Z-sections) of cleared tomato roots 5 days post inoculation (DPI) with *Fo*. Root samples were stained with a mix of Propidium iodide (PI; red) and fluorescein isothiocyanate-conjugated wheat germ agglutinin (FITC-WGA; green) to visualize respectively plant cell walls and fungal chitin. Representative intra- or inter-cellular hyphae are indicated by white dotted line squares or white arrowheads, respectively. Experiments were repeated three times with similar results. Scale bar, 100 µm.

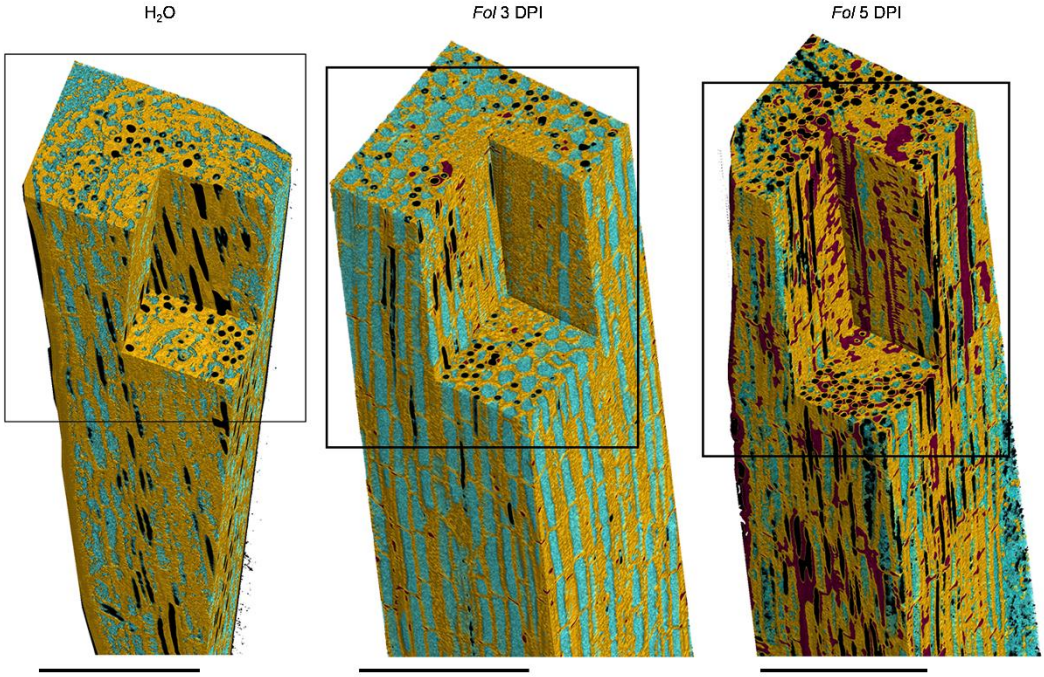

Extended Data Fig. 5. Phase contrast micro-CT imaging reveals progressive colonization, tissue damage and embolism in *Fusarium oxysporum* infected tomato roots. Representative 3D renderings of synchrotron X-ray micro-CT scans showing tomato roots either mock-treated (H_2O) or infected with *Fo* at 3- and 5-days post inoculation (DPI). Yellow: cell walls; light blue: cytoplasm; black: air spaces; magenta: fungal hyphae. Scale bar, 0.25 mm.

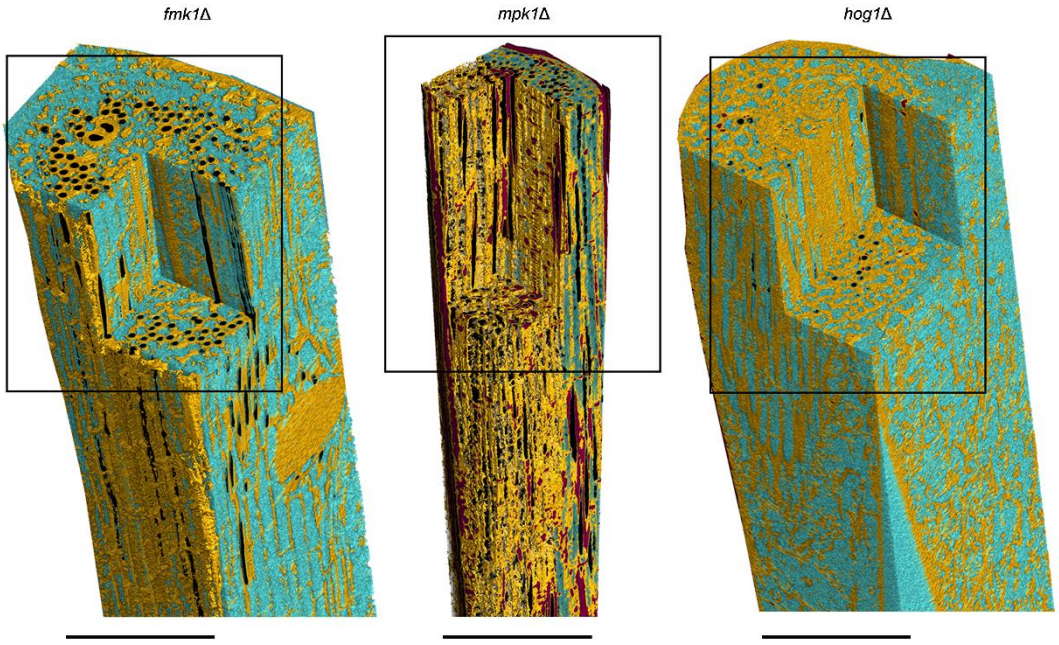

Extended Data Fig. 6. Phase contrast micro-CT imaging reveals differential colonization patterns by *Fusarium oxysporum* MAPK mutants in tomato roots. Representative 3D renderings of synchrotron X-ray micro-CT scans showing tomato roots infected with *Fo* MAPK mutant strains (*fmk1*Δ, *mpk1*Δ, and *hog1*Δ) at 5 days post inoculation (DPI). Yellow: cell walls; light blue: cytoplasm; black: air spaces; magenta: fungal hyphae. Scale bar, 0.25 mm.

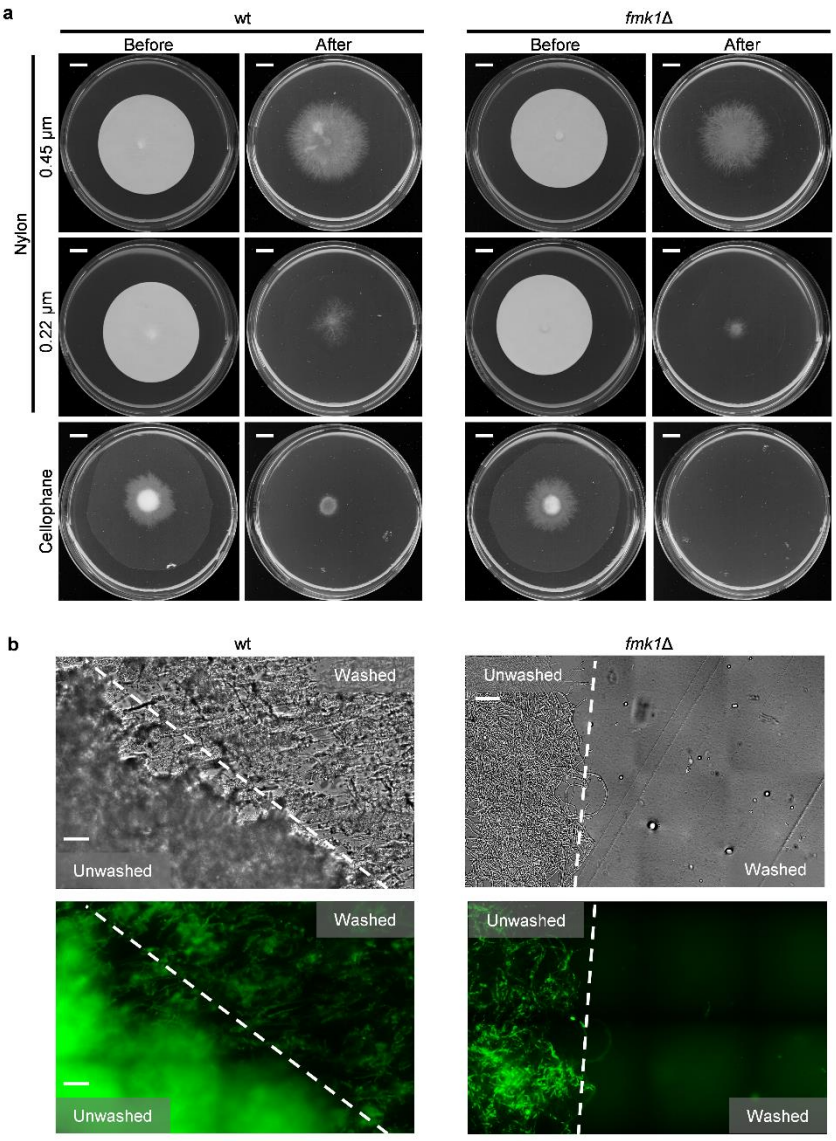

Extended Data Fig. 7. Fmk1 MAPK governs surface attachment and force-mediated substrate invasion in *Fusarium oxysporum*. **a**, Penetration assays through nylon membranes (0.45 or 0.22 µm pores) or cellophane (poreless) comparing wt and *fmk1*Δ strains. Fungal colonies were grown on minimal medium (MM) and imaged on top of the indicated membranes (Before) and again 24h after membrane removal (After) to assess penetration. Scale bar, 1 cm. **b**, Differential interference contrast (DIC) and maximum intensity projection (MIP; combining 80 Z-sections) images of wild-type and *fmk1*Δ strains stained with fluorescein isothiocyanate-conjugated wheat germ agglutinin (FITC-WGA; green) after growth on a cellophane membrane. After 3 d of incubation on a MM plate, one half of the cellophane sheet was vigorously washed under tap water (bottom right) or left unwashed (top left), stained and imaged. Note the presence of enlarged bulbous cells strongly attached to cellophane in wt but not *fmk1*Δ. Scale bar, 50 µm.

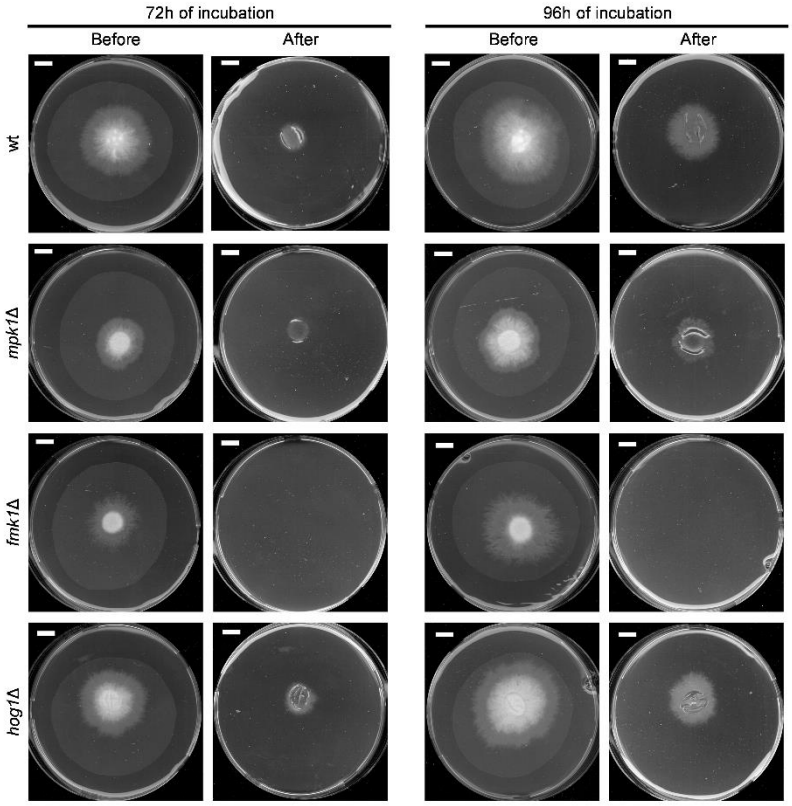

776
777
778
779
780 **Extended Data Fig. 8. Comparative cellophane penetration by *Fusarium oxysporum* wild-type and MAPK**
781 **mutant strains at different time points.** Penetration assays through cellophane membranes comparing wt and MAPK
782 mutant strains (*fmk1*Δ, *mpk1*Δ, and *hog1*Δ). Fungal colonies were grown on minimal medium (MM) and imaged on
783 top of cellophane membranes (Before) after 72h or 96h of incubation, and again 24h after membrane removal (After)
784 to assess penetration. Note the progression of penetration capacity between the two time points in the wt, *mpk1*Δ, and
785 *hog1*Δ, but not in the *fmk1*Δ mutant strain. Scale bar, 1 cm.

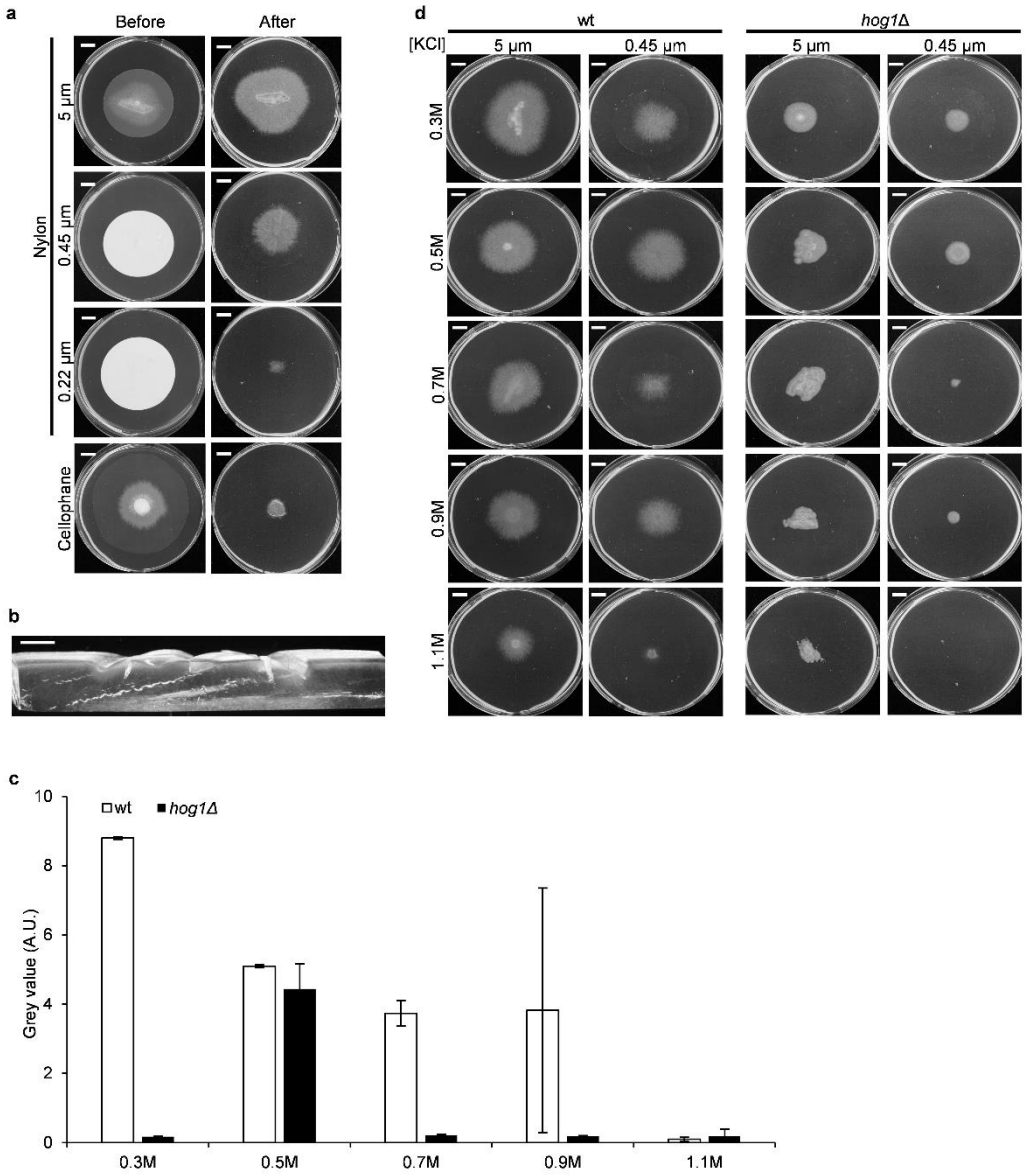

Extended Data Fig. 9. Hog1 MAPK is required for submicrometric hyphal adaptation to osmotic stress in *Fusarium oxysporum*. **a**, Penetration assays through nylon membranes (5, 0.45 or 0.22 µm pores) or cellophane (poreless) with the *hog1*Δ mutant. Fungal colonies were grown on minimal medium (MM) and imaged before (Before) and 24h after membrane removal (After). Scale bar, 1 cm. **b**, Cross-sections of the growth substrate following cellophane penetration assays with the *hog1*Δ mutant at 4 days post inoculation (DPI). The image reveals organized substrate deformation patterns beneath the *hog1*Δ colony, indicating preserved mechanical force transmission despite impaired osmoadaptive capacity. Scale bar, 1 mm. **c**, Quantification of penetration efficiency through nylon membranes (0.22 µm pores) at different KCl concentrations. Mean gray values (in arbitrary units) were measured in areas under fungal colonies 72h after inoculation. Note, the wild-type strain shows significantly higher penetration compared to *hog1*Δ at both hyperosmotic and hypoosmotic conditions. **d**, Membrane penetration under osmotic stress in wt and *hog1*Δ strains. Colonies were grown on MM with increasing KCl concentrations (0.3-1.1 M, generating osmotic pressures from 1.38-5.06 MPa) and imaged 24h after membrane removal. Note progressive loss of penetration with increasing osmotic pressure in *hog1*Δ but not in the wt strain. Scale bar, 1 cm.

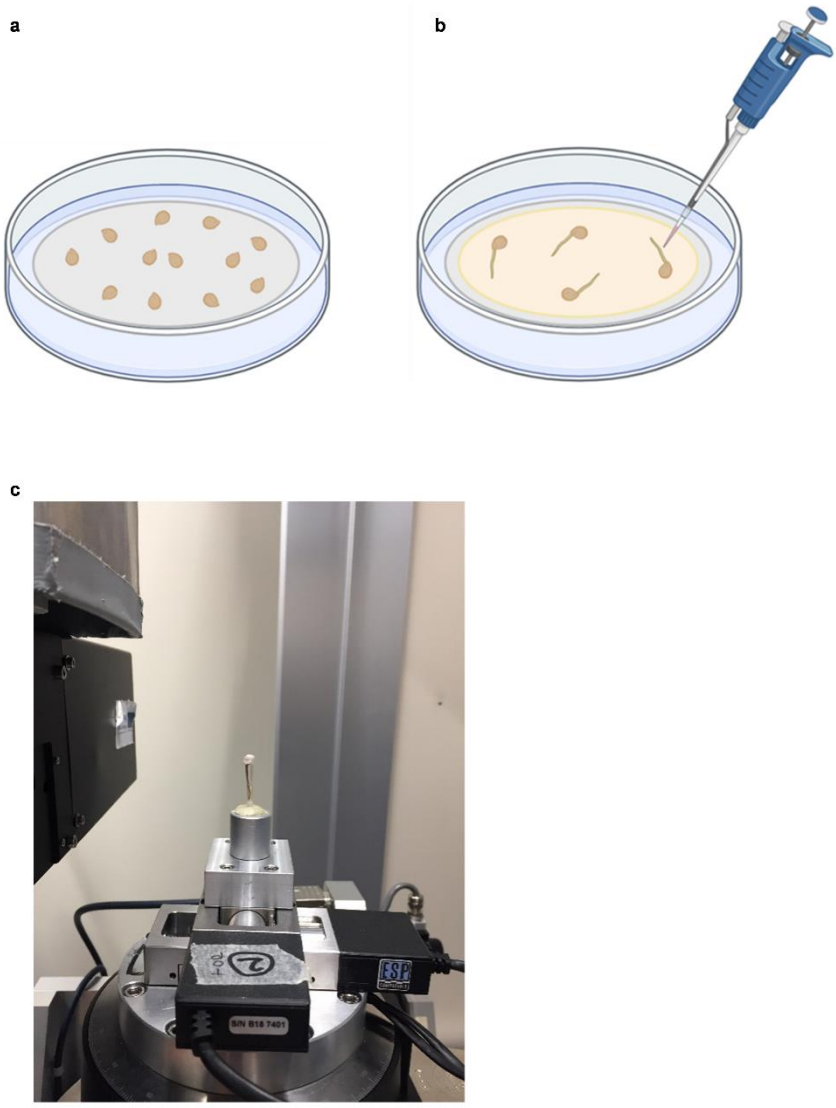

Extended Data Fig. 10. Experimental setup for analyzing fungal-root interactions using X-ray microtomography. a, Seed germination: surface-sterilized *S. lycopersicum* seeds were germinated on sterile filter paper (moistened with sterile distilled water) in 90-mm Petri dishes under controlled conditions (28°C, darkness). **b**, Root inoculation system: four-day-old tomato seedlings were transferred onto sterile cellophane membranes overlaid on water-saturated filter paper. Roots were spot-inoculated with 50 µL of *Fo* microconidia suspension (5×10^5 conidia). **c**, Sample mounting configuration at the SYRMEP beamline: the inoculated root segment, contained within a sealed polypropylene pipette tip, was secured in a cylindrical aluminum holder positioned on high-precision translation and rotation stages for phase contrast synchrotron X-ray microtomography imaging.

Extended Data Tables

Extended Data Table 1. ***Fusarium oxysporum*** **strains used in this study.**

Strain	Genotype	Gene function	Reference
FGSC 4287	wild type		[42]
fmk1Δ	*fmk1::PHLEO*	MAPK	[28]
mpk1Δ	*mpk1::HYG*	MAPK	[25]
hog1Δ	*hog1:: HYG*	MAPK	[27]
4287-*3X-Fo-mClover3*	*3X-Fo-mClover3::HYG*	Fluorescent cytoplasmic reporter	[31,32]

Supplementary Files

This is a list of supplementary files associated with this preprint. Click to download.

- Descriptionofadditionalsupplementaryitems.pdf
- ExtendeddataFig.10.tif
- SupplementaryVideo2.avi
- ExtendeddataFig.3.tif
- ExtendeddataFig.2.tif
- ExtendeddataFig.8.tif
- ExtendeddataFig.9.tif
- ExtendeddataFig.42.tif
- ExtendeddataFig.7.tif
- ExtendeddataFig.1.tif
- ExtendeddataFig.6.tif
- ExtendeddataFig.5.tif
- SupplementaryVideo1.gif